The 13th Hypervelocity Impact Symposium

Analytic Ballistic Performance Model of Whipple Shields

J. E. Miller[a,b]*, M. D. Bjorkman[b], E. L. Christiansen[c], and S. J. Ryan[d]

aCASSMAR, University of Texas at El Paso, 500 W. University Ave., El Paso, TX 79968
bJacobs, NASA Johnson Space Center, 2101 NASA Parkway, Houston, TX 77058
cNASA Johnson Space Center, 2101 NASA Parkway, Houston, TX 77058
dDefence Science and Technology Organisation, 506 Lorimer Street, Fishermans Bend, VIC 3207, Australia

Abstract

The dual-wall, Whipple shield is the shield of choice for lightweight, long-duration flight. The shield uses an initial sacrificial wall to initiate fragmentation and melt an impacting threat that expands over a void before hitting a subsequent shield wall of a critical component. The key parameters to this type of shield are the rear wall and its mass which stops the debris, as well as the minimum shock wave strength generated by the threat particle impact of the sacrificial wall and the amount of room that is available for expansion. Ensuring the shock wave strength is sufficiently high to achieve large scale fragmentation/melt of the threat particle enables the expansion of the threat and reduces the momentum flux of the debris on the rear wall. Three key factors in the shock wave strength achieved are the thickness of the sacrificial wall relative to the characteristic dimension of the impacting particle, the density and material cohesion contrast of the sacrificial wall relative to the threat particle and the impact speed. The mass of the rear wall and the sacrificial wall are desirable to minimize for launch costs making it important to have an understanding of the effects of density contrast and impact speed. An analytic model is developed here, to describe the influence of these three key factors. In addition this paper develops a description of a fourth key parameter related to fragmentation and its role in establishing the onset of projectile expansion.© 2015 Published by Elsevier Ltd. Selection and/or peer-review under responsibility of the Hypervelocity Impact Society.

Keywords: multi-shock shield, catalogued debris, fabric shield

1. Introduction

Ballistic limit equations have been developed to define the failure limits of a MMOD shield, generally in terms of projectile diameter (or mass), impact velocity, and angle [1]. Within the range of impact velocities relevant for Earth-orbiting spacecraft, three distinct regions of penetration phenomenology have been identified for light-weight two wall shields: low velocity, intermediate (shatter) velocity, hypervelocity [2]. While each of these regimes are well observed, with extensive empirical methods to describe the first two regions, differences in impactor materials, configurations of shields and questions about the limitations of the attainable impact speeds create concerns for extrapolations beyond the body of evidence despite increased complexity. Hydrodynamic simulations are effective in extending the predictive capability of shield performance; however, they are sometimes too costly in time and resources for consideration by programs especially in the initial phases when the design is most effectively optimized. As a consequence, spacecraft design engineers are most assisted by pulling the basic principles of the hydrodynamic

* Corresponding author. Tel.: +1-281-244-8093; fax: +1-281-483-3908.
E-mail address: joshua.e.miller@nasa.gov.

simulation along with material properties into a tractable form that can be accomplished with minimal computational requirements.

To this end, an analytical effort to understand these regions has been undertaken that involves solving mass and momentum equations for a Lagrangian description of the projectile and the walls of the Whipple shield to yield a transmitted particle velocity of the material based on whether or not the wall is optimum (shock wave reaches the rear of the threat particle before the rarefaction wave) or non-optimum (shock wave strength decreases prior to arrival at the back of the threat particle). With respect to the sacrificial wall, once the average transmitted particle velocity is known an energy balance can be performed to determine the rate of the lateral release of the threat projectile and target material prior to the impact of the rear wall. With the diffuse mass and transmitted particle velocity of the impact remnants, a new calculation of the terminus particle velocity through the rear wall can be performed; therefore, by varying the initial conditions at the front wall, a set of transmitted conditions that arrest the impact remnants can be solved for iteratively yielding critical projectile size as a function of impact conditions.

This paper documents the derivation of this analytical model. The paper discusses the constitutive properties that are necessary to account for the Whipple shield performance in the analytic model. The developed analytic model are then compared to a generalized database of over fifteen hundred impact tests that have been recently developed with various impacting materials, front wall materials, and obliquities; along with, direct comparison to scaling tests that isolate strain rate behavior for both aluminum and steel projectiles.

2. Materials & Methods

A large database of over one and a half thousand impacts into double wall Whipple shields has recently been developed that form the basis for the evaluation of the analytic ballistic performance model developed here [3]. The database consists of a large number of shield configurations from optimum to non-optimum front wall configurations, from sub-centimeter to meter separation between the walls, to a wide range of materials from aluminum to lead and polymers to ceramics. As such, in addition to the geometrical description of the impact process that is developed here, the material mechanical and thermal properties of the diverse array of materials is also needed.

To develop the necessary material properties, an analysis of the collection of the shock wave response of materials in the international shock wave database has been performed [4]. The mechanical properties are derived using the traditional shock wave relationships from the linear kinematic form relating the shock wave velocity, U, to the particle velocity, u, by way $U = s\,u + c$. As it is important to account for thermal aspects of the release of shock wave compressed material, the recently proposed non-linear shock wave slope, s, [5] is used in this analysis where the slope is a function of the particle velocity and can be empirically determined from the shock wave data in the frame of reference of the driven material ($U - u$ versus u) [6] using the relationship:

$$s = s_\infty + \delta s\, Exp\left[-\frac{u}{\delta u}\right] \tag{1}$$

where s_∞, δs and δu are empirical parameters. Along with the zero intercept, c, which is approximately the bulk sound speed in the material, these parameters are sufficient to describe up to first order phase transitions seen in materials. Higher order phase transitions like those in iron and quartz in the lower shock wave strengths require more complexity, and in this work they are ignored as there activation energy and/or the prevalence of porosity in natural meteoroid materials diminish their importance for the typical impact energies of orbital and exo-orbital collisions.

Figure 1 shows characteristic curve fits transferred to the laboratory frame of reference for aluminum and iron as solid black lines relative to the shock wave data points shown in black that are compiled in the international shock wave database. In each of the cases, it can be seen that the approach of modeling the slope with an added exponentially decaying non-linear term approximates the gathered data well. Each plot is labeled with the equation describing the loci of shock wave data. This approach has been used to develop shock wave relations for other metals and polymers needed for the impact database.

In addition to the shock wave parameters, the shock wave database also archives lateral release wave speed measurements [4]. In these experiments an impactor with a width narrower than the field of observation impacts a target material of broader width [7]. A rarefaction wave starts to relieve stress, due to the finite width, and by measuring the extent of the relief at breakout of the target material for the known thickness of the impactor a release wave speed can be inferred. Some of these archived datapoints are shown in Figure 1 in blue for aluminum and iron. Although for some cases this release wave speed is reasonably approximated by the shock wave velocity, it is easily

seen for other materials this approximation is not as good especially as the particle velocity becomes greater than the zero intercept velocity.

a)

$$u(1.2 + 0.3\,e^{-0.117647u}) + 5.3$$
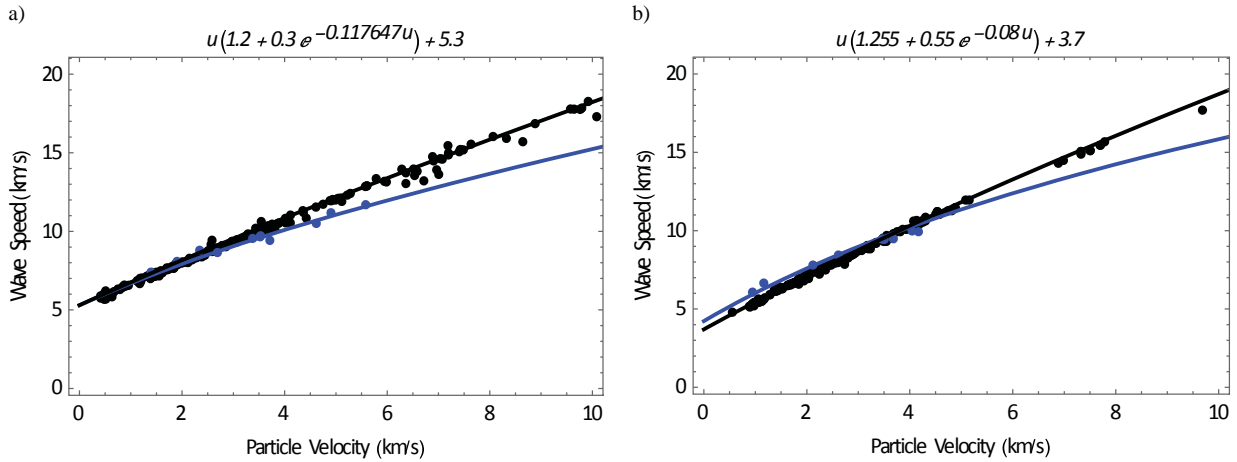
b)

$$u(1.255 + 0.55\,e^{-0.08u}) + 3.7$$

Figure 1 Shock and release wave speeds for characteristic materials of importance of impacts a) aluminum and b) iron

Using these archived data, a better approximation of the release wave speed is arrived at by subtracting the wave kinetic energy from the shock wave energy, $1/2\,(U^2 - u^2)$, yielding the waves thermal energy, upon taking the square root is the thermal speed. The release wave speed is actually related to the isentropic speed requiring the inclusion of an adiabatic coefficient, γ. While only explicitly true for ideal gases, analysis of the archived data has shown that the adiabatic coefficient for shock waves can be approximated by $\gamma \cong 2\,s - 1$ where s is the slope of the linear dependence of the shock wave velocity on the particle velocity. Putting these together yields an approximate description of the adiabatic release wave speed

$$c_R \cong \sqrt{(s - 1/2)\,((s\,u + c)^2 - u^2)}. \tag{2}$$

The release speeds are also shown in Figure 1 for each of the materials as the blue curve. As can be seen this description of the release wave speed provides much better agreement to the archived data, and owing to the relationship dependence on shock wave parameters, it is possible to forecast what the release wave speed for materials that have not been measured like cadmium might be as shown.

3. Theory

To start to address the impact database, the interaction of the solid sphere with the first wall of the two wall shield requires considering the two counter-propagating shock waves that are induced in the materials as shown in the density contours of Figure 2. In this figure, three points in the impact process from hydrodynamic simulations of a 1.4 mm spherical aluminum impact on a 0.6 mm aluminum plate at 9 km/s are shown in the three frames. Figure 2a shows the density contour just as the impactor is about to hit the aluminum plate; Figure 2b and Figure 2c show the density contours just as the shock wave is about to exit the aluminum plate and the impactor, respectively. For a spherical impactor the shock wave initiates at the point of impact and begins moving through the impactor. The shock wave in a spherical impactor is continually reinforced from fresh plate material producing a relatively planar shock wave in the impactor as can be seen in Figure 2b. As the rarefaction wave from the front surface reaches the backward propagating shock wave, the shock wave begins weakening; however, concentration of shock wave energy due to the converging back half of the impactor continues to maintain a relatively planar shock wave throughout the passage of the shock wave in the impactor. As such, the shock wave within the spherical projectile is reasonably well modeled as a planar shock wave in a finite material.

Owing to the approximately planar nature of the shock wave in the impactor, a finite thickness one dimensional approach to modeling the interaction is acceptable for describing the projectile state in the midst of the first wall. In this description the projectile of diameter, d_i, and density, ρ_i, hits the first wall of the double wall shield that has an areal density, $\overline{m_w}$, which is the product of the wall thickness and wall density, at the impact velocity, u_i. To combine the projectile and first wall in the one dimensional sense, an equivalent areal density for the projectile can be found by taking the ratio of the mass of the projectile to its frontal area yielding, $\overline{m_i} = 2/3\ \rho_i\,d_i$. Upon the termination of

the projectile's interaction with the first wall, the impact remnants then move on toward the second wall of the double shield with an areal density, $\overline{m_W}'$, at the transmitted velocity u_o.
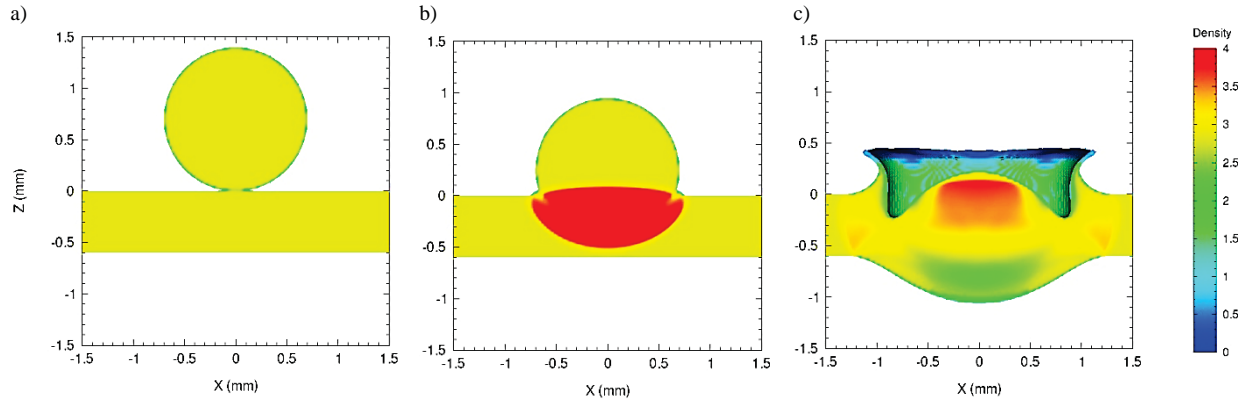

Figure 2 Stages of a solid spherical impactor on a plate a) prior to impact b) prior to shock wave exit at the front of the plate and c) prior to shock wave exit of impactor

The impact results in counter propagating shock waves in the projectile and the wall with a continuous pressure and particle velocity across the interface. These counter propagating shock waves in the frame of reference of the target wall represents the loci of stable pressures at a particle velocity for the projectile and the wall. The loci of stable shock wave states in a material are approximately given for strong shock waves by the product of the initial density, the shock wave velocity and the particle velocity. The impedance matched stable particle velocity resulting from the impact can be found with the material kinematic parameters yielding:

$$u_\infty = \frac{(\rho_i\,c_i+\rho_W\,c_W+2\,\rho_i\,s_i\,u_i)-\sqrt{(\rho_i\,c_i+\rho_W\,c_W)^2+4\,\rho_i\,\rho_W\,(s_i\,c_W+s_W\,(s_i u_i+c_i))\,u_i}}{2\,(\rho_i\,s_i-\rho_W\,s_W)}, \tag{3}$$

where the i and W subscripts indicate the impactor and wall, respectively. As can be readily seen, this velocity is only dependent on the materials and the impact velocity.

This equilibrium particle velocity is for the impact of two semi-infinite materials; yet, the projectile and the wall both have finite dimensions, so the resultant transmitted velocity of impact remnants is not necessarily this semi-infinite value. The time that the shock wave from the impact propagates through the wall is given by $t_W = \overline{m}_W/(\rho_W\,(s_W\,u_\infty + c_W))$, where $\overline{m}_W$ and ρ_W are the areal density, mass per unit area, and the density, mass per unit volume, of the wall, respectively. A similar relationship can be derived for the impactor given by $t_i = \overline{m}_i/(\rho_i\,(s_i\,(u_i - u_\infty) + c_i))$. When the time for the shock wave to propagate through the projectile is greater than the target wall, the resulting average velocity of the impact remnants is greater than u_∞ and can be approximated by a mass average

$$u_o = \frac{\overline{m}_W}{\overline{m}_i+\overline{m}_W}\left(\frac{\hat{R}_W+1}{\hat{R}_W}\right)u_\infty + \frac{\overline{m}_i}{\overline{m}_i+\overline{m}_W}\left(\frac{\overline{m}_i\,\hat{R}_W-\overline{m}_W}{\overline{m}_i\,\hat{R}_W}\right)u_i, \tag{4}$$

where the dimensionless impedance parameter $\hat{R}_W$ is given by

$$\hat{R}_W = \frac{\rho_W\,(s_W\,u_\infty+c_W)}{\rho_i\,(s_i\,(u_i-u_\infty)+c_i)}. \tag{5}$$

For the case that the transit time through the projectile is less than the transit time of the shock wave in the target wall, the shock wave begins to release through the projectile and slows down as a decaying shock wave. A model has been developed for this case from a Lagrangian form of the combination of the continuity, the aforementioned kinematic form of the equation of state, and the momentum conservation equation [8]. Starting with the momentum conservation equation in a frame at rest with the particle along the propagation direction

$$\overline{m}\,\frac{du}{dt} = -\left(\rho_0\,U\,u + \frac{1}{2}\,\rho^*(u-U)^2\right) \tag{6}$$

the left-hand side is the momentum flux changes experienced by the projectile and the accelerated target wall material, and the right-hand side is the hydrodynamic force acting on the control volume. The term $\rho^* = \rho_i\,U/(U - u)$, and is

the shock wave compressed density. This momentum balance equation can then be solved from the position when shock wave departs the projectile to the release from the target wall yielding:

$$u_o = \left(u_\infty + \frac{c_W}{s_W+1}\right)\left(\frac{\bar{m}_i}{\bar{m}_i+\bar{m}_W}(1+\hat{R}_W)\right)^{\frac{s_W+1}{2}} - \left(u_F + \frac{c_W}{s_W+1}\right) \tag{7}$$

where u_F is the failure velocity needed to overcome the tensile strength of the target wall. This minimum velocity can be determined equating the kinetic energy to the integrated tensile energy of the wall material.

After exiting the front wall, the shock wave compressed material decompresses and expands as can be seen in the simulation of the 1.4 mm spherical aluminum projectile on the 0.6 mm aluminum wall shown in Figure 3a. The shock wave compressed material that moves at the transmitted speed, u_o, also decompresses at the release speed, c_R. This expansion ultimately diffuses the projectile material over a larger area of the rear wall making it a crucial parameter in understanding the overall performance of the shield system. To model this expansion, the expansion rate for each material, ω, is determined from the ratio of the lateral release wave speed from Eqn. 2 to the sum of the transmitted velocity and the lateral release wave speed as illustrated in Figure 3b. As the material only expands if the thermal energy exceeds the mechanical work required to break apart the material, the ratio is multiplied by the fraction of the impact energy that resides in the material as excess thermal energy resulting in the expression,

$$\omega = \frac{c_R}{c_R+u_o}\left(1-\left(\frac{u_o}{u_i}\right)^2 - \left(\frac{N_S\,\sigma_S\,\epsilon_c}{1/2\,\rho_i\,u_i^2}\right)\right) \tag{8}$$

where N_S, σ_S and ϵ_c are the number of spall zones at the horizon of the transition from brittle to ductile spall, the brittle spall stress and the critical strain which is about 0.15, respectively [9]. If no excess thermal energy is available, then the projectile is merely plastically compressed, and assuming it expands laterally to about its original density results in a flattened diameter of about the square root of compressed density larger than prior to impact, $\sqrt{\rho^*/\rho_i}$.
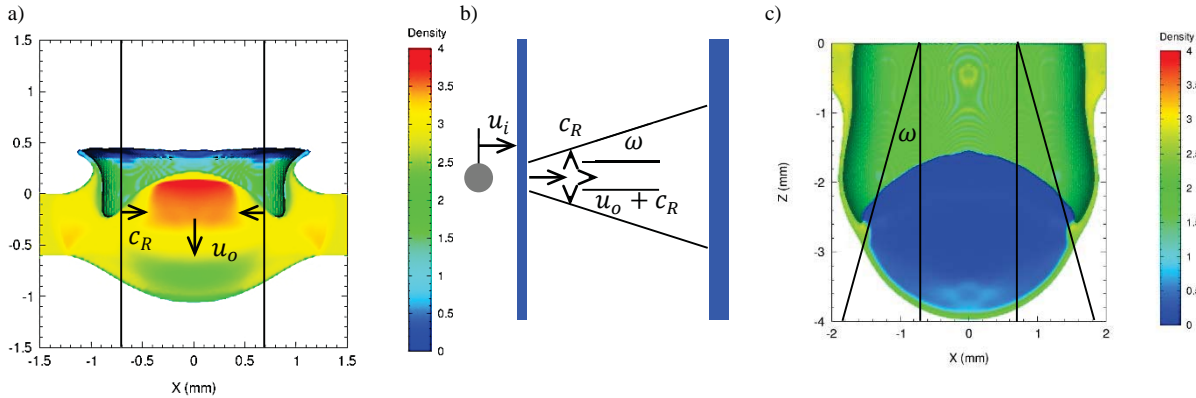

Figure 3 Debris cloud expansion a) simulated view of the waves moving within the shock wave compressed projectile, b) expansion illustration of the debris cloud about the center of mass and c) evolved simulation of the expansion of the compressed projectile in the vacuum of the gap

The continuation of the simulation of the 1.4 mm projectile impact onto the 0.6 mm after a three times propagation is shown in Figure 3c. As can be seen in the simulated view, with this expansion set at initial decompression the peak areal density, product of the density and the depth of material, continues to decline through the diffusion process. Modeling this diffusion process by using the expanded radius as a fixed point of a Gaussian curve, the peak areal density of the debris cloud impacting the rear wall is given by:

$$\bar{m}_o = \bar{m}_i\left(\frac{r_i}{\sqrt{\rho^*/\rho_i}\,r_i+\omega_i\,S_{FP}}\right) + \bar{m}_W\left(\frac{r_i}{\sqrt{\rho^*/\rho_i}\,r_i+\omega_W\,S_{FP}}\right) \tag{9}$$

where S_{FP} is distance traveled by the debris cloud along the flight path and the projectile and the wall material are allowed to have differing rates of expansion. This material then interacts with the rear wall in the same manner as the front wall with the exception that if it is necessary for the rear wall to stop the material, then the decaying shock wave solution must be satisfied. Solving Eqn. 7 for the impacting areal density yields:

$$\bar{m}_o = \frac{\hat{u}'}{\left(1+\hat{R}_W'\right)-\hat{u}'}\,\bar{m}_W' \tag{10}$$

where $\hat{R}_W{'}$ is the same quantity as that in Eqn. 5 with rear wall parameters, and $\hat{u}'$ is given by:

$$\hat{u}' = \left(\frac{u_F{'} + \frac{c_W{'}}{s_W{'}+1}}{u_\infty{'} + \frac{c_W{'}}{s_W{'}+1}} \right)^{\frac{2}{s_W{'}+1}} \qquad (11)$$

where again the prime indicates a rear wall quantity and $u_\infty{'}$ is the solution of Eqn. 3 using the average debris velocity with the initial density and kinematic properties of the projectile. The combination of Eqn. 9 and 10 can then be solved for the diameter of the projectile that exceeds the spallation limit of the rear wall yielding:

$$d_i = \frac{3}{2} \left(\frac{\bar{m}_W{'}}{\rho_i} \frac{\hat{u}' \left(\sqrt{\rho^*/\rho_i} + 2\,\omega_i S_{FP}/d_i \right)}{\left(1 + \hat{R}_W{'} \right) - \hat{u}'} - \frac{\bar{m}_W}{\rho_i} \left(\frac{\sqrt{\rho^*/\rho_i} + 2\,\omega_i S_{FP}/d_i}{\sqrt{\rho^*/\rho_i} + 2\,\omega_W S_{FP}/d_i} \right) \right). \qquad (12)$$

While the derivation has been based on normal impacts, modifications can be made to transform distances like $\bar{m}_W$, S_{FP} and $\bar{m}_W{'}$ to their flight path value by dividing by the cosine of the angle between the normal of the wall and flight path, which is the impact obliquity, θ_i, for the first wall and a transmitted obliquity given by:

$$\theta_o = Arcsin \left[\frac{\bar{m}_i}{\bar{m}_i + \bar{m}_W} Sin[\theta_i] \right]. \qquad (13)$$

4. Discussion

The geometrical equations of the previous section along with the material properties are sufficient to describe shield performance while allowing great versatility, albeit, at the cost of complexity. The transcendental nature requires iterative solution schemes. These equations have been solved for the more than one and a half thousand double wall impacts in the impact database with the comparative residuals shown in Figure 4 [3]. In Figure 4a the difference between the tested projectile versus the calculated critical diameter is plotted against the normal component of the projectile velocity to the shield for tests where the shield failed to stop the projectile. As rendered, accurate modeling of the test is made when the test point is above the ordinate zero. As can be seen, this ballistic performance model achieves good agreement with 87.2% accuracy, and 95.4% of the fails are contained within 0.5 mm below or above the ballistic performance curve. Similarly, in Figure 4b the same difference is shown for the tests where the shield stopped the projectile with accurate modeling when the test point is below the ordinate zero. Here too it can be seen that there is good agreement between the ballistic performance model's representation of passes at 86%, and 93.0% of the passes are contained within 0.5 mm above or below the ballistic performance curve.
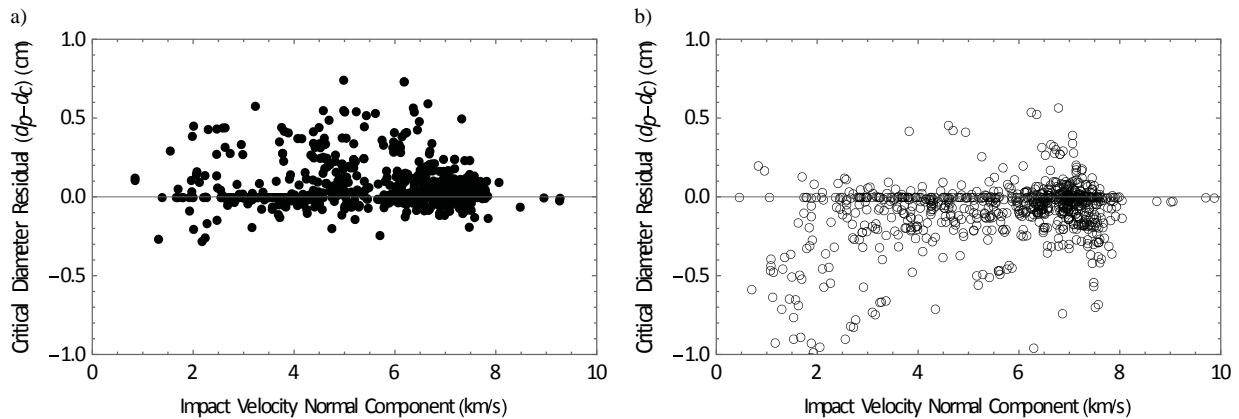

Figure 4 Residuals (tested diameter less calculated diameter) from the impact database by test outcome a) test shield failed and b) test shield passed

While this rendition of the model relative to the test database gives a reasonably good view of the extensibility of the model, Figure 4 lacks a view of how close the model's performance curve comes to demonstrating the shield ballistic limits. To show this aspect of the performance Figure 5 shows ballistic performance curves for four different shield configurations. In Figure 5, like Figure 4, tests that resulted in a shield failure are shown as filled disks, and tests that resulted in a shield defeating the projectile are shown as open disks. Figure 5a through Figure 5c show a

comparison of the ballistic model relative to the recent data from normal impacts in a scaling study of double wall Whipple shields for Al2017-T4 projectiles [10]. Figure 5a is the shield performance of a representation of a US International Space Station Laboratory Module full-scale shield. This shield system consists of a 1.27 mm Al6061-T6 first wall separated by 10.16 cm from a 3.175 mm Al2219-T87 rear wall. In Figure 5b and Figure 5c the shield performance of 0.46-scale and quarter-scale versions of the base full-scale shield are shown, respectively. The testing performed during this series produced quality results very near the ballistic limit of the shields with failure of detached spall common in the vicinity of shield passes; consequently, performance curves accurately representing the performance should be close to the tested points. In addition to the examples from the scaling series of tests, Figure 5d shows the shield performance of a similar US Laboratory Module shield against SS440C steel projectiles. This shield consists of a 2 mm first wall separated from a 4.8 mm rear wall. The total depth of the shield system is 11.4 cm. This figure compares the performance for both normal impacts (in black) and for impacts 45° to normal (in blue).
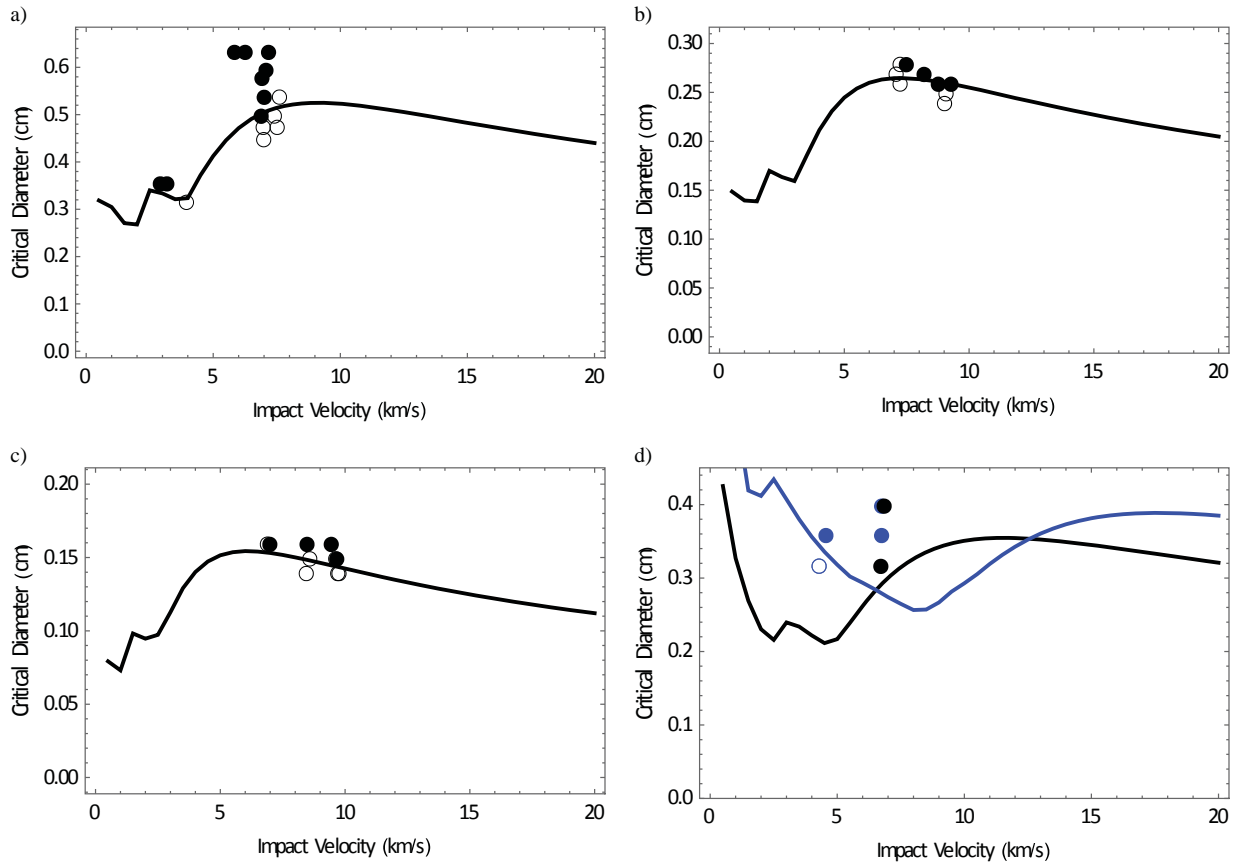

Figure 5 Shield ballistic performance examples for a) ISS US laboratory module representative shield against aluminum b) 0.46-scale against aluminum c) quarter-scale against aluminum, and d) ISS US laboratory module representative shield against steel.

As can be seen in Figure 5, the ballistic performance model follows the same trend across scales and materials. At low impact velocities, the projectile and the holed out front wall remain in-tact and impact the rear wall with increased momentum flux with increased impact velocity. For the non-optimum shield case, like the set of shields represented in this figure, the stresses in the front wall are much higher than in the projectile, and at still higher impact velocities the impact energy in the front wall exceeds the fracture energy required to hold the wall together. As a consequence, the front wall expands and is a reduced contributor at the peak momentum flux on the rear wall, which results in an increase of performance until the penetrating mass on the rear wall is dominated by the projectile. At sufficiently high impact velocity the impact energy in the projectile also exceeds the fracture energy of the projectile, and the projectile also expands resulting in increased shield performance with increased impact velocity. The relationship of the expansion velocity to the particle velocity results in a limit to the amount the projectile and front wall can spread; hence, results in a peak for performance increase when it is assumed that the rear wall is shock wave compressed by

the projectile material. As both the impact energy relative to the fracture energy and the limit of expansion are related to shield characteristics, the transitions these two regions define are related to the shield configuration.

5. Conclusion

The analytical model documented here represents the effort to achieve a method of modeling the performance of double wall Whipple shields that captures the essential elements of hydrodynamic simulations in a form that can be used within risk assessments of shield concepts, especially early in the conceptual design phase. To achieve applicability to a broad range of potential materials, specific constitutive properties that are necessary to account for the Whipple shield performance have been developed. The developed analytic model has been compared to a generalized database of over one and a half thousand impact tests and direct comparison to high quality tests of both aluminum and steel projectiles.

The model provides good agreement with many of the test records that have been recorded. Despite the broad range of projectile and first wall materials in the records, the records are focused on an aluminum alloy rear wall and do not provide additional comparison of the performance of the rear wall. Similarly, there is limited data to support the fragmentation properties of many materials and understanding these properties better could yield improved results. These uncertainties result in the continued necessity to verify results by test and simulation; however, the derivatives of this model could improve shield design, and the improved extrapolation should yield more rapid and inexpensive shield development and verification. Continued refinement of assumptions, especially with respect to those that affect performance outside the currently testable range, are warranted to adapt to changing requirements of use.

References

[1] E. L. Christiansen, MMOD Handbook, 2009.

[2] E. L. Christiansen, Meteoroid/Debris Shielding, 2003.

[3] S. Ryan, "Advanced neural networks for characterizing Whipple shield performance," *Int J Imp Engng,* vol. 01/2013, no. 56, pp. 1-70, 2013.

[4] "Shock wave database," [Online]. Available: http://teos.ficp.ac.ru/rusbank/index.php?text=3. [Accessed 2014].

[5] M. Knudson, "Shock Compression of Quartz to 1.6 TPa: Redefining a Pressure Standard," *Phys Rev Letter,* vol. 103, no. 22501, 2009.

[6] G. Kerley, "The Linear US-uP Relation in Shock-Wave Physics," Kerley Technical Services, 2006.

[7] Y. B. Zeldovich, Physics of Shock Waves and High-Temperature Hydrodynamic Phenomena, Dover Publications, 2002.

[8] J. E. Miller, "Ballistic performance of porous-ceramic, thermal protection systems," *Int. J. Imp. Engng.,* vol. 56, pp. 40-46, 2012.

[9] D. E. Grady, "The spall strength of condensed matter," *J. Mech. Phys. Solids,* vol. 36, no. 3, pp. 353-384, 1988.

[10] A. J. Piekutowski, "Effects of Scale on the Performance of Whipple Shields for Impact Velocities Ranging from 7 to 10 km/s," *Procedia Engng.,* vol. 58, pp. 642-652, 2013.

[11] E. S. Hertel, "Comparison of analytic Whipple bumper shield limits with CTH simulations," Sandia National Laboratory SAND92-0347, 1992.